Nanoscale

Structural and Mechanical Characteristics of Exosomes from Osteosarcoma Cells Explored by 3D-Atomic Force Microscopy

Journal:	*Nanoscale*
Manuscript ID	NR-ART-12-2020-009178.R1
Article Type:	Paper
Date Submitted by the Author:	26-Feb-2021
Complete List of Authors:	Yurtsever, Ayhan; Kanazawa University - Kakuma Campus Yoshida, Takeshi; Kanazawa University Behjat, Arash; Kanazawa University - Kakuma Campus Araki, Yoshinori; Kanazawa University Hanayama, Rikinari; Kanazawa University Fukuma, Takeshi; Kanazawa University - Kakuma Campus

Journal Name

ARTICLE TYPE

Cite this: DOI: 00.0000/xxxxxxxxxx

Structural and Mechanical Characteristics of Exosomes from Osteosarcoma Cells Explored by 3D-Atomic Force Microscopy†

Ayhan Yurtsever,*[a] Takeshi Yoshida,[a,b] Arash Badami Behjat,[a] Yoshihiro Araki,[b,c] Rikinari Hanayama,[a,b] and Takeshi Fukuma*[a]

Received Date
Accepted Date

DOI: 00.0000/xxxxxxxxxx

Exosomes have recently gained interest as mediators of cell-to-cell communication and as potential biomarkers for cancer and other diseases. They also have potential as nanocarriers for drug delivery systems. Therefore, detailed structural, molecular, and biomechanical characterization of exosomes is of great importance for developing methods to detect and identify the changes associated with the presence of cancer and other diseases. Here, we employed three-dimensional atomic force microscopy (3D-AFM) to reveal the structural and nanomechanical properties of exosomes at high spatial resolution in physiologically relevant conditions. The substructural details of exosomes released from three different cell types were determined based on 3D-AFM force mapping. The resulting analysis revealed the presence of distinct local domains bulging out from the exosome surfaces, which were associated with the exosomal membrane proteins present on the outer surface. The nanomechanical properties of individual exosomes were determined from the 3D-force maps. We found a considerably high elastic modulus, ranging from 50 to 350 MPa, as compared to that obtained for synthetic liposomes. Moreover, malignancy-dependent changes in the exosome mechanical properties were revealed by comparing metastatic and nonmetastatic tumor cell-derived exosomes. We found a clear difference in their Young's modulus values, suggesting differences in their protein profiles and other exosomal contents. Exosomes derived from a highly aggressive and metastatic k-ras-activated human osteosarcoma (OS) cell line (143B) showed a higher Young's modulus than that derived from a nonaggressive and nonmetastatic k-ras-wildtype human OS cell line (HOS). The increased elastic modulus of the 143B cell-derived exosomes was ascribed to the presence of abundant specific proteins responsible for elastic fiber formation as determined by mass spectroscopy and confirmed by western blotting and ELISA. Therefore, we conclude that exosomes derived from metastatic tumor cells carry an exclusive protein content that differs from their nonmetastatic counterparts, and thus they exhibit different mechanical characteristics. Discrimination between metastatic and nonmetastatic malignant cell-derived exosomes would be of great importance for studying exosome biological functions and using them as diagnostic biomarkers for various tumor types. Our findings further suggest that metastatic tumor cells release exosomes that express increased levels of elastic fiber-associated proteins to preserve their softness.

Introduction

Extracellular vesicles (EVs), particularly exosomes, have recently gained interest due to their emerging roles as mediators of intercellular communication and as novel biomarkers of cancers and other diseases, including their potential to be used as drug delivery vehicles[1–3]. Exosomes are nano-sized (typically between

[a] WPI Nano Life Science Institute (WPI-Nano LSI), Kanazawa University, Kakuma-machi, Kanazawa 920-1192, Japan. E-mail:yurtsever@staff.kanazawa.u-ac.jp; fukuma@staff.kanazawa.u-ac.jp; Fax: +81-76-234-4632; Tel: +81-76-234-4564

[b] Department of Immunology, Kanazawa University Graduate School of Medical Sciences, 13-1 Takara, Kanazawa, Ishikawa 920-8640, Japan

[c] Department of Orthopaedic Surgery, Kanazawa University Graduate School of Medical Sciences, 13-1 Takara, Kanazawa 920-8640, Japan

† Electronic Supplementary Information (ESI) available: Additional experimental details for NTA and TEM measurements; AFM images of ruptured exosomes in water; size distribution comparison of exosomes isolated from HOS and 143B cell lines; Young's modulus distributions of 143B and HOS cell-derived-exosomes; additional AFM images of live HOS and 143B cells; additional details for extraction of mechanical properties of live HOS and 143B cells; proteomic profiling of parental cells that secrete HOS-and 143B-exosomes; gene ontology (GO) enrichment analysis of exosomes. See DOI: 00.0000/00000000.

30-150 nm in diameter) lipid bilayer-enclosed membrane vesicles released from a wide variety of living cells, including cancer cells, into the extracellular environment, and are present in most bodily fluids such as blood, saliva, breast milk, urine, malignant ascites, and seminal fluids[4–7]. These circulating vesicles, formerly thought to be "cellular garbage bags" for throwing out redundant proteins and non-functional cellular components[8], are now recognized as important mediators of intercellular communication through the transfer of different types of functional cargoes from parent to neighboring and/or distant cells[9,10]. Besides their participation in the regulation of normal biological processes, several lines of evidence suggest that exosomes play an essential role in several pathological disorders, including tumor progression, metastatic spread, and cardiovascular disease[11–16]. Through the transfer of their molecular cargoes into recipient cells, exosomes can promote tumor progression and spread[17,18].

The molecular cargo of exosomes is highly diverse and comprises a specific mixture of bioactive proteins/enzymes, lipids, receptors, and genetic material (mRNAs, miRNAs, and DNAs) that can vary depending on the cell type and its metabolic status[11,19–21]. They are also reported to convey various immune-regulatory, disease-related, immunosuppressive, and tumor progression proteins between cells (Figure 1). Therefore, the structure and molecular composition of exosomes can harbor a wealth of information associated with the physiological and pathological states of parental cells. Given that exosomes contain cell type-specific biomolecules, it has been suggested that tumor-derived exosomes may differ from those of healthy ones in terms of their structural, molecular, and biomechanical characteristics[22–24]. Several studies have shown that tumor-derived exosomes are enriched in specific proteins[25,26], and their expression levels are closely related to tumor development[27], which makes them potentially important diagnostic biomarkers. Because of their potential as novel biomarkers and their easy and quick accessibility, the biophysical and molecular characterization of these vesicles could enable the early detection of changes associated with tumors and other diseases.

Because of their small size and morphological and compositional diversity[28,29], it is extremely challenging to characterize exosomes and study their ultra-structural details. Various analytical techniques, including field emission scanning electron microscopy (FESEM), cryo-electron microscopy (cryo-EM), and transmission electron microscopy (TEM), have been exploited to determine the structure, morphology, and size distribution of exosomes[30–34]. While FESEM and cryo-EM images have revealed a homogeneous round morphology for exosomes[30,35], TEM observation performed after fixation and negative staining has shown a distorted 2D "cup-shaped" morphology without further structural details[32,33,36].

As an alternative and complementary method to those mentioned above, atomic force microscopy (AFM) offers nondestructive, label-free characterization of biological materials in their native environments at single-molecule sensitivity and subnanometer resolution[37]. In addition, it allows us to probe the nanomechanical properties of biological materials[38–40], allowing for better understanding of the mechanobiological properties of cells and nano-sized vesicles, and providing insights into the structure-function relationships of small vesicles[41]. Despite its suitability, there are still only a few studies that have used AFM for exosome characterization[23,30,42–44]. In addition, these studies have been limited in resolution and could not provide ultrastructural details of exosomes at the sub-vesicular level under physiological conditions. More importantly, the potential interplay between the structural/mechanical characteristics of exosomes and their contribution to malignancy has not been fully explored[23,45]. Differences in the structure and molecular composition of these vesicles can affect their mechanical properties and functionality. Understanding the morphological, nanomechanical, and biochemical properties of exosomes at the single-vesicle or sub-vesicular level is of critical importance in determining their functions, for instance in tumor progression and metastasis. In addition, elucidating the mechanical properties of exosomes is crucial to understanding their deformation properties and stability against mechanical perturbations, which are important for their possible use as drug carriers.

Here, we report the use of 3D-AFM under in-liquid conditions to reveal the structural and nanomechanical characteristics of exosomes derived from three different cell types: a highly aggressive and metastatic murine osteosarcoma (OS) cell line (LM8), a highly aggressive and metastatic k-ras-activated human OS cell line (143B)[46], and a nonaggressive and nonmetastatic k-ras-wildtype human OS cell line (HOS)[47]. The 3D-AFM force maps acquired over individual exosomes revealed a non-homogeneous granular-like morphology with distinct local regions, which could be attributed to the presence of proteins such as receptors that are exposed to the outer surface of the exosome membrane. Nanomechanical properties of exosomes were obtained from the measured 3D-force maps. A relatively high Young's modulus value, ranging from 50 to 350 MPa on average, was found compared to that of synthetic liposomes[48,49], indicating the importance of exosomal proteins in exosome mechanics. Furthermore, we found a clear difference in the mechanical properties between nonmetastatic and metastatic tumor cell-derived exosomes. Exosome proteomic analysis using mass spectrometry, ELISA, and western blotting indicated the enrichment of certain proteins specific to elastic fiber assembly. These groups of proteins were found to be highly enriched in 143B cell-derived exosomes compared to the HOS cell-derived exosomes. This may explain the observed mechanical differences between metastatic and nonmetastatic tumor cell-derived exosomes. We further examined the mechanical properties of the parent cells that secrete HOS and 143B exosomes. The results showed a decrease in the Young's modulus of 143B cells compared to that of HOS cells, confirming widely accepted results. Cell-based ELISA indicated that the elastic-fiber associated proteins—which were highly expressed in 143B exosomes—were significantly less expressed in metastatic parent 143B cells than in nonmetastatic HOS cells. Our findings thus suggest that metastatic tumor cells may preserve their softness by releasing certain proteins through exosomes.

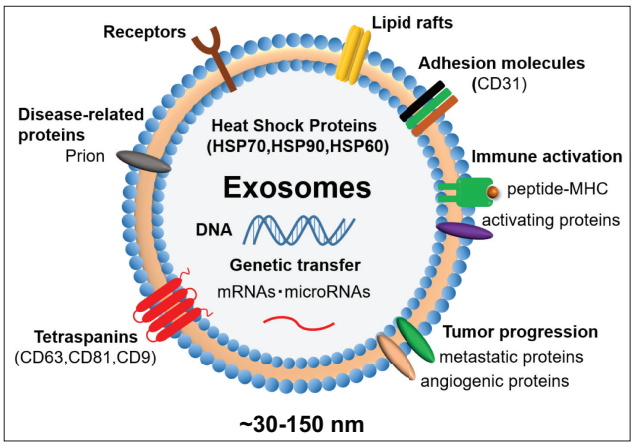

Fig. 1 Schematic showing the typical structure and biomolecular content of exosomes. The payload of exosomes can include proteins, receptors, adhesion molecules, lipids, miRNAs, mRNAs, DNAs, and other bioactive substances. They can also carry various immuno-regulatory, disease-related, immunosuppressive, and tumor progression proteins.

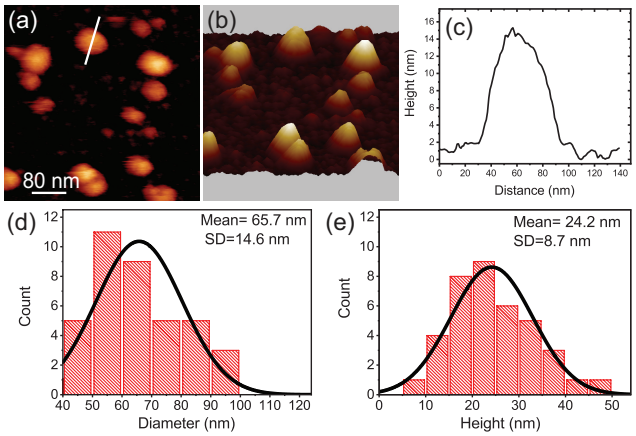

Fig. 2 Physical characterization of exosomes by AFM. (a) A representative AFM topography image of LM8 cell-derived exosomes immobilized on an APTES-modified mica substrate, which was observed in TBS buffer, showing individual round-shaped vesicles of different sizes ranging from 40 to 100 nm. (b) Three-dimensional rendering of the topographic image shown in panel a. (c) A representative topographic cross-sectional profile (determined by averaging the height with a ten-pixel width) taken along a line passing through the center of the vesicle marked in a, displaying dimensions of approximately 14 nm in height and 64 nm in diameter. Size distribution of exosomes secreted from LM8 cell lines: (d) the width and (e) the height distribution. We note that the diameter of the vesicles measured by AFM corresponds to the width of the height profile passing through the center of the vesicles at the base.

Results and discussion

Structural characterization of exosomes in liquid using 3D-AFM

Exosomes were captured using the T-cell immunoglobulin domain and mucin domain-containing protein 4 (Tim4)-immobilized magnetic beads[50], as described in Materials and Methods. It has been demonstrated that Tim4 proteins exhibit a high binding affinity for the phosphatidylserine exposed on the external leaflet of exosomes[51]. The specific interactions between Tim4 proteins and phosphatidylserine molecules, in the presence of Ca^{2+} ions, enabled the isolation of intact exosomes from various cell culture media and body fluids. It has been demonstrated that exosomes purified using this method have a higher purity than those extracted using other conventional isolation methods[50]. The isolated exosomes were then characterized structurally by nanoparticle tracking analysis (NTA), TEM, and AFM. The size distribution of exosomes was analyzed by NTA using NanoSight analysis (Supporting Information (SI), Figure S1). The mean diameter of the vesicles measured by NTA showed values in the range of 100 to 130 nm, which is consistent with the size of exosomes determined in previous studies using NTA. The TEM measurements acquired through the use of negative staining revealed typical 2D cup-shaped, shrunken vesicles surrounded by electron-dense lipid-bilayered membranes, but further structural details were not resolved (SI, Figure S2), consistent with previous findings[44,52]. The observed cup-shaped (i.e., a central depression) morphology of exosomes is thought to be an artifact caused by the chemical fixation, dehydration, and staining of the sample, as stated earlier; thus, it does not reflect the real exosome morphology. Moreover, TEM analysis confirmed the presence of particles with various sizes, and no other non-exosomal contaminants or protein aggregates were observed in this preparation process, suggesting high purity of the samples.

We performed frequency modulation AFM (FM-AFM) measurements to assess the structural/morphological aspects of exosomes under aqueous conditions. Exosomes were imaged in TBS buffer or ultrapure water. Each exosome fraction was placed onto a freshly cleaved mica substrate exposed previously to the 3-aminopropyltriethoxysilane (APTES) vapors (to reverse the surface charge). After rising with ultrapure water, the exosome samples were then subjected to AFM observation (see Materials and Methods for details). The AFM data revealed that the exosomes immobilized onto the APTES-modified mica substrate appeared as isolated vesicles with characteristic rounded morphology with no information about their substructural details, in line with previous reports for exosomes released in other bodily fluids[30,53]. A representative AFM topography image displayed in Figure 2a and 2b shows hydrated vesicles with varying sizes without any aggregation and deformation (i.e., partially or fully collapsed vesicles). The dimensions of these vesicles derived from the LM8 cell line are summarized in Figure 2d and 2e, showing a histogram of the width (d) and height (e) of the vesicles, which was derived from various samples. It can be seen that the typical diameters ranged from 40 to 100 nm, with an average diameter of 65.7 nm in width, and height values in the range of 10 to 50 nm with an average height of 24.2 nm, as determined based on AFM cross-sectional analysis (see Figure 2c). This range of height values is compatible with the values for solid surface-supported membrane vesicles in liquid conditions. This suggests that the chemical fixation did not cause much structural distortion. Indeed, the vesicle heights were higher (*ca.* 15 nm) than those measured using tapping mode and peak force AFM imaging[43]. We note that strong silanization of the mica substrate by APTES can lead to a rupture of spherical vesicles, resulting in the formation of flattened-bilayer patches with an average thickness of 4.5–5 nm,

the release of genetic material, and adsorption onto the substrate (SI, Figure S3).

Substructure of exosomes

To probe the substructural details of isolated exosomes, we employed the 3D-AFM-based force measurement method developed by Fukuma *et al.*[54]. A schematic drawing in Figure 3a demonstrates the 3D-AFM force mapping experiment on a nanovesicle immobilized on a solid substrate. In this method, the tip is scanned both vertically and laterally to probe the interaction forces acting between the tip and surface in the 3D interfacial space. The (z) tip position is modulated with a fast sine wave during the lateral tip movement. During the tip lateral scans, Δf is recorded for each tip position while the average tip-sample distance is regulated in such a way that the average value of Δf set-point is kept constant. A 3D-force map with high spatial resolution can be constructed by recording the force field acting on the tip for each vertical displacement. The main difference between 2D- and 3D-AFM is the use of Z modulation signal during 2D XY scans. The other 3D-AFM methods have no tip-sample regulation during the tip XY scans and are extremely slow[55]. The fast acquisition speed of 3D-AFM makes it suitable for imaging in liquid environments, where non-linear drift is always present and is extremely difficult to prevent[56]. The acquired map of the 3D force fields can be used to determine the local elastic properties of exosomes, such as Young's modulus and stiffness[40]. Thus, 3D-AFM enables the simultaneous acquisition of a structural/morphological and nanomechanical property map, and thereby specific morphological and molecular variations can be correlated to the mechanical property changes.

After locating the vesicles, we carried out 3D-force mapping on selected single vesicles. To ensure that the vesicles were not deformed or ruptured, we performed a set of AFM imaging and 3D-force mapping sequentially on particular vesicles that showed no evidence of changes in the exosome morphology and position. A typical force map collected on a nanovesicle isolated from the LM8 cell line is shown in Figure 3. Figure 3b displays the 3D rendering of an exosome immobilized on the APTES-modified mica substrate as acquired in TBS buffer. The resulting 3D-force map obtained on this particular vesicle is depicted in Figure 3c, revealing a non-homogeneous, granular-like morphology with distinct local regions bulging out from the exosome surface. The 2D-force profile in the vertical Z-Y plane, obtained along the white-dashed trajectory shown in Figure 3c, enabled the distinction between different subdomains (Figure 3e). A topographic height variation of 4-5 nm can be readily seen between two protruding features in the 2D-force profile (Figures 3e and 3f). This can be attributed to the heterogeneous presence of exosomal proteins displayed on the outer leaflet of the exosome membrane.

In a previous study using amplitude modulation AFM (AM-AFM), Sharma *et al.*, reported a trilobed structure with a central depression for saliva-derived exosomes[30]; the authors attributed this structural feature to mechanical perturbation due to high force imaging conditions. Contrary to the previous observations of saliva-derived exosomes, we did not observe such a

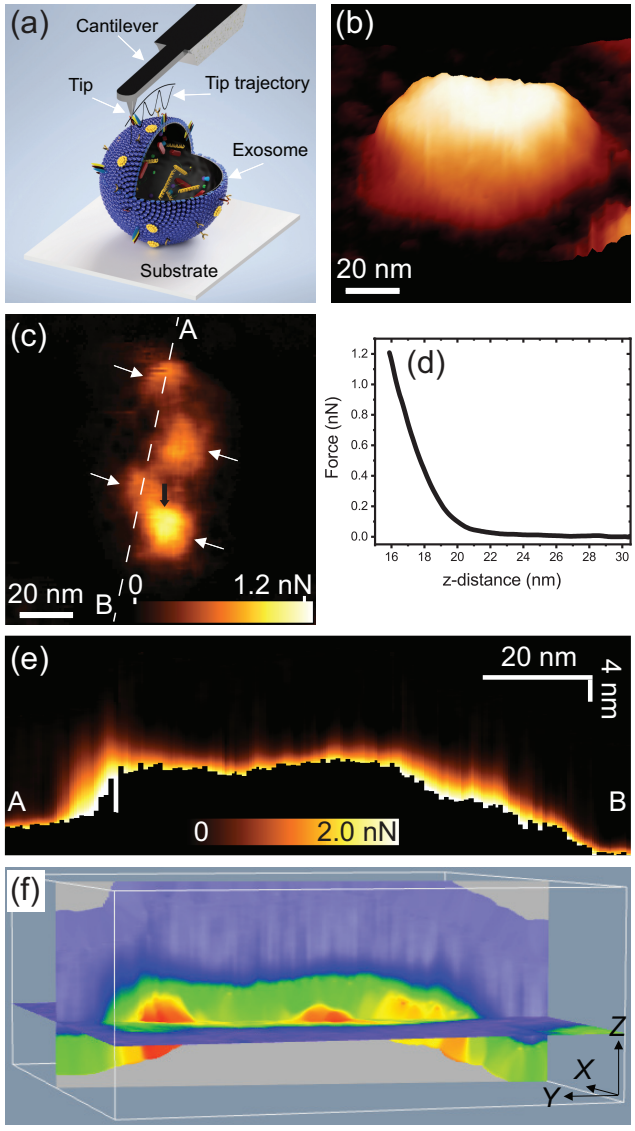

Fig. 3 3D-force map collected on exosomes isolated from LM8 cell lines in buffer conditions. (a) Schematic representation of the 3D-AFM force mapping experiment showing the AFM probe located above the top of an exosome immobilized on a solid substrate. (b) 3D rendering of an AFM image of an individual exosome with a dimension of 74 nm in diameter and 21 nm in height, acquired simultaneously with the 3D-force map in panel c. (c) 3D-force map acquired over the exosome shown in panel b, revealing the distinction of different substructural domains (highlighted by white arrows) on the exosome surface. Four bright protruding features appear over the top of the vesicle. (d) A typical single force-distance curve extracted from the position marked with a black arrow in panel c, indicating that there is no rupture event. (e) 2D-force map profile in the Z-X plane obtained along the white-dashed line shown in panel c. A topographic height difference of 4-5 nm can be seen between two protruding features in the 2D-force profile. (f) 3D-visualization of the force map by Voxler software, highlighting the surface features along the same plane as in e. Two protruding features (red) can be clearly seen. The force mapping area has a dimension of 112 nm $\times$ 112 nm and is divided into grids of 256 $\times$ 256 pixels. The z-scale in panel b is 0-23.2 nm.

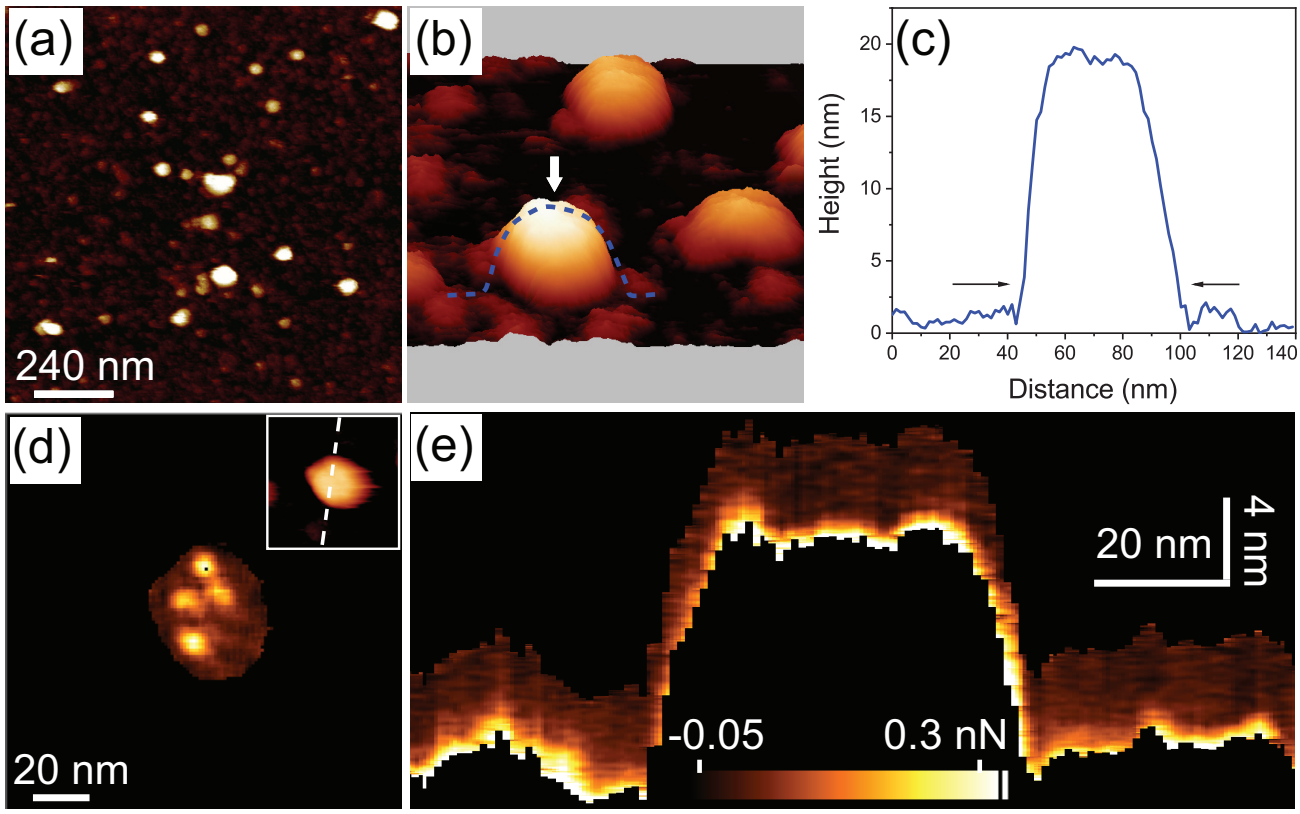

Fig. 4 3D-force map collected from exosomes isolated from the 143B cell line in buffer conditions. (a) (1.2μm $\times$ 1.2μm) An overview AFM image of exosomes adsorbed on an APTES-modified mica substrate, showing various round-shaped objects with different sizes ranging from 40 to 120 nm. (b) 3D rendering of an AFM image of exosomes. An exosome marked by a white arrow was used for the force mapping analysis. (c) The corresponding height profile along the dashed line highlighted in panel b, showing an approximately 60 nm diameter and 18 nm high exosome. (d) 2D-force map reconstructed from the 3D-force mapping data, where four distinct protruding features are clearly visible at the center-top region of the vesicle. The color scale was adjusted for better visualization of the topmost part of the vesicle. Inset: AFM topographic image of the exosome recorded simultaneously with the 3D force map. (e) 2D force mapping profile in the X-Z plane obtained along the path shown in the inset image in panel d. Three protruding features can be identified in the force profile. The horizontal color bar represents force in nN.

substructural organization in exosome morphology. This difference might be because the indentation in our case was limited to a few nanometers of distance that correspond to the size of the lipid bilayer. Furthermore, the previous study showed that exosomes were ruptured during imaging in the air for a force value of around 5 nN[30]. A typical single force-distance curve extracted from the 3D-force dataset in Figure 3c is displayed in Figure 3d, where the data do not show any rupture events, which would be evidenced from the appearance of discontinuities in the force-distance curves. This indicates that the bilayers were not ruptured during force mapping, and thereby the vesicle morphology in AFM topography images remained essentially unchanged.

Similar 3D-force measurements were performed on exosomes derived from highly metastatic 143B and nonmetastatic HOS cell lines. The sizes of these nanovesicles, as determined by AFM, were found to be almost identical to those from the LM8 cell line (SI, Figure S4). The AFM characterization of exosomes from different samples yielded an average size of approximately 60-70 nm in diameter for both cell lines, in agreement with NTA results (SI, Figure S1). Figure 4a shows an overview AFM topography image of the 143B cell-derived exosomes as acquired in ultrapure water. They exhibited a characteristic rounded shape morphology with various sizes, similar to LM8 exosomes. We could not find obvious morphological differences between LM8, HOS, and 143B cell-derived exosomes. A 3D-force map with the corresponding 2D-force profile acquired on an individual exosome is shown in Figure 4d and 4e, respectively. An exosome with a size of about 60 nm in diameter and 18 nm in height was selected for the force mapping analysis (a line profile across the vesicle is shown in Figure 4c). Although the topographic images do not exhibit much substructural detail (Figure 4a and 4b), the 3D-force map—acquired over the exosome marked by an arrow in Figure 4b—revealed the presence of four distinct rounded shape features bulging out from the exosome surface, similar to the LM8-derived exosomes. We note that the color scale in Figure 4d was adjusted for better visualization of the topmost part of the vesicle. The 2D (Z-X) force profile, taken along the dashed line shown in the inset image of Figure 4d, revealed a distinction between different domains in the exosome surface (Figure 4e). The force profile analysis provided a topographic height variation of 1.5-2 nm between the bright features with a lateral size of 10-15 nm. As in the case of the LM8 exosomes, these bright features are presumably membrane-associated proteins exposed on the outer surface and/or other exosomal contents confined in the exosomes. Of

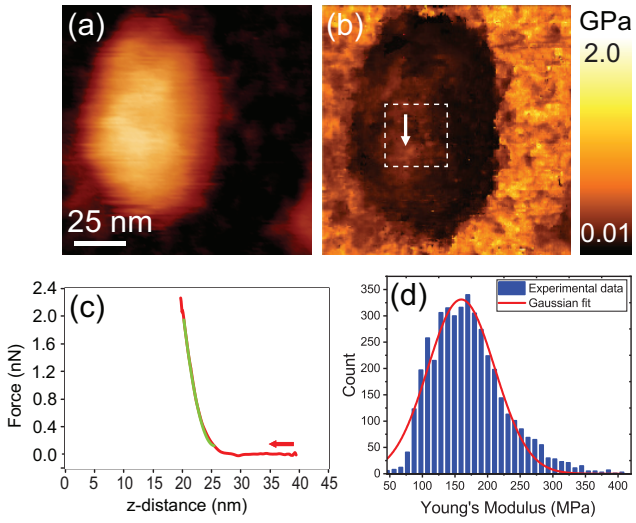

Fig. 5 Mapping the mechanical properties of exosomes. Representative topography (a) and corresponding Young's modulus map (b) of an exosome derived from the LM8 cell line. The Young's modulus map includes 256 × 256 pixels. The area occupied by the exosome appears dark and is characterized by a lower value of elastic modulus. (c) A typical force-distance ($F(z)$) curve (red) with the fitted Sneddon model curve (green) obtained from the position marked with a white arrow in the elasticity map. The indentation distance used for the model fit was limited to a few nm that corresponds to the size of a lipid bilayer. (d) Histogram showing the distribution of Young's modulus values measured for an LM8 exosome. The histogram was derived from an area covering typically 30 × 30 nm^2 with 64 × 64 pixels, located on the central part of the vesicle as highlighted with a white dashed square. The solid red line represents the fitted Gaussian function. The mean Young's modulus value of the histogram was 159.6 ± 51.3 MPa. We note that the topography map shown in panel a was recorded simultaneously with the 3D-AFM force map (SI, Figure S5b).

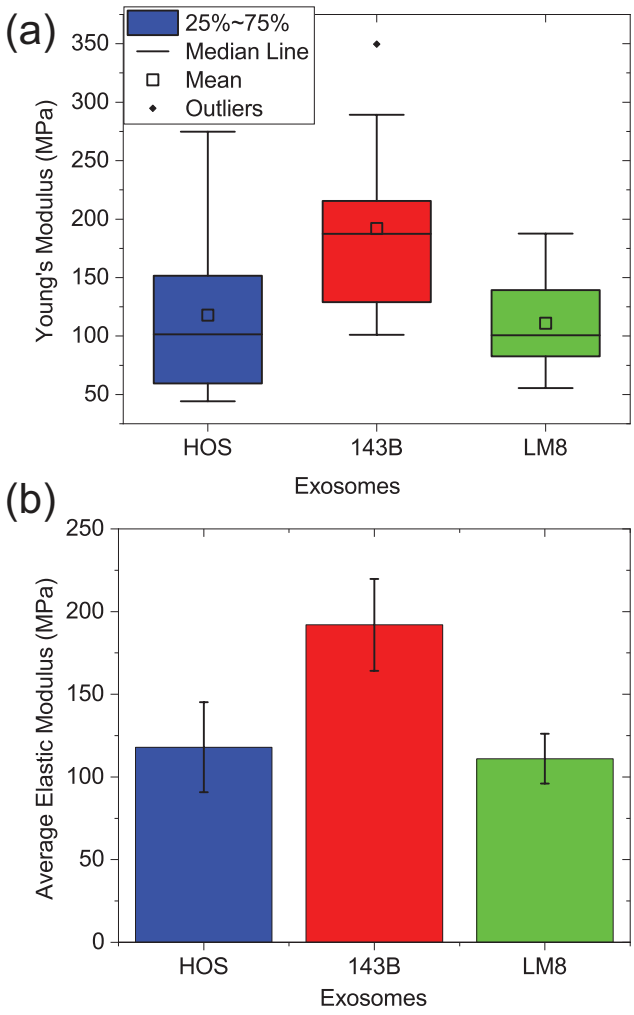

Fig. 6 Comparison of elastic moduli. (a) Box-and-whisker plots of the Young's modulus distributions of HOS, 143B, and LM8 exosomes. (b) Histogram bars represent the mean elastic moduli of HOS, 143B, and LM8 exosomes collected from AFM Young's modulus maps for various vesicles. The data are presented as the mean ± standard error of the mean (SEM), as indicated by the error bars. The measured average Young's modulus values are 117.9 ± 27.2, 191.9 ± 27.8, and 111 ±15 MPa for HOS, 143B, and LM8 cell-derived exosomes, respectively.

note, the force maps acquired on different exosomes show some variation in exosome morphology at the molecular level, where the number of protruding features and their location appear to be different (SI, Figure S5b). The different appearances of the exosomes in high-resolution 3D-AFM images may be explained by: (i) the reorganization of membrane-associated proteins and receptors on the exosome surface after adsorption on a solid surface, (ii) the exosomes purified from a cell line may have diverse composition and morphology, as has been previously reported[28].

Mapping the nanomechanical properties of exosomes.

In the next step, we explored the biophysical properties of exosomes derived from LM8, HOS, and 143B cell lines. It has been well established that the biological functions of cells, membrane enclosed vesicles, and other biomolecules are closely related to their structural and mechanical characteristics in normal and diseased conditions[40]. The mechanical properties of nano-sized membrane vesicles, i.e., their elasticity/stiffness, play an essential role in several biological processes, e.g., interaction with cell surfaces, cellular signaling, cellular uptake, adhesion, transport, vesicle generation, and drug delivery[45,57–59].

The nanomechanical properties of exosomes were determined through the use of a contact mechanics model provided by Sneddon *et al.*[60]; see Materials and Methods for details. This contact mechanics model has been widely used to explore the biophysical properties of soft biological samples, including unilamellar egg yolk phosphatidylcholine (EggPC) vesicles and other membrane vesicles[61–63].

A representative example of a Young's modulus map acquired on an exosome isolated from the LM8 cell line is shown in Figure 5. Figure 5 shows the topography (a) and the corresponding Young's modulus (b) map of an exosome immobilized on an APTES-modified mica substrate. The area occupied by the exosome appears darker and is characterized by a lower value of Young's modulus than the supporting substrate. An example of the typical force-distance curve (red) with the fitted Sneddon model curve (green) is shown in Figure 5c. The fit range was limited to the indentation distances of about a few nanometers that correspond to the size of a lipid bilayer, thus allowing us to probe

the mechanical properties in the elastic regime. The histogram shown in Figure 5d indicates the distribution of the Young modulus values compiled from the central part of the vesicle covering an area of about 30 × 30 nm^2 with 64 × 64 pixels. Gaussian fitting to the histogram of the calculated Young's modulus values revealed an average value of 159.6 ± 51.3 MPa (Figure 5d). The average Young's moduli of LM8 exosomes ranged from 50 to 180 MPa (Figure 6a). This variability presumably implies the fact that exosomes derived from the same type of cell might have diverse biochemical compositions[64]. However, we cannot exclude the possibility that exosomes with different sizes have different subpopulations, which exhibit different biomechanical properties, as has been reported recently[65]. We note that the Young's modulus distributions obtained from the central part of the vesicles (covering an area of 30 × 30 nm^2) are generally unimodal and can be fitted by a Gaussian function. However, the distributions—derived from the relatively large surface area covering almost all of the area enclosing an individual exosome—are multimodal and can be fitted by multiple Gaussian functions (SI, Figure S5d). This heterogeneity in Young's modulus distribution can also be seen in the resulting Young's modulus map. Distinct domains with different modulus values can readily be seen, reflecting the local mechanical differences.

We next compared possible differences in the mechanical properties of metastatic and nonmetastatic tumor cell-derived exosomes purified from 143B and HOS cells, respectively. These two cell lines were derived from the same parental TE-85 cells, a human OS line, and thus the differences in their exosome mechanical properties should reflect differences in their malignancy. Similar Young's modulus maps, as demonstrated in Figure 5, were acquired over individual exosomes derived from 143B and HOS cells (SI, Figure S6). The resulting modulus values for 143B and HOS cell-derived exosomes ranged from about 100 to 350 MPa with an average value of 192 MPa for the former, and 50 to 200 MPa with an average value of 118 MPa for the latter (Figure 6a). The variability observed in the modulus values points toward heterogeneity in exosome mechanical properties, as also observed in LM8 exosomes. A comparison of the average Young's modulus values between highly aggressive metastatic (143B cell-derived) and nonaggressive, nonmetastatic (HOS cell-derived) exosomes is presented in Figure 6b. We found that the Young's modulus of metastatic tumor cell-derived exosomes, on average, is higher than that of nonmetastatic tumor cell-derived exosomes (Figure 6b). The elastic moduli of LM8-derived exosomes are also included in Figure 6b for comparison. Although the LM8-derived exosomes originated from a highly aggressive metastatic murine OS cell line, they exhibited lower Young's moduli compared to the metastatic 143B cell-derived exosomes with identical sizes. This implies that the mechanical properties of exosomes depend on their cell of origin.

A comparison with reported Young's modulus values of natural membrane vesicles reveals that our data lie within the range of reported values[59]. Calò *et al.*[59] have reported the importance of the composition and structure for the mechanical properties of small nano-sized natural vesicles. It has been suggested that the membrane proteins present on small nanovesicles mainly determine their modulus properties. Therefore, we conclude that the observed high values of Young's moduli imply an important role for membrane-associated proteins in exosomes mechanics, and the observed differences in the Young's modulus values between metastatic and nonmetastatic tumor-derived exosomes could be explained by differences in their exosomal protein cargoes.

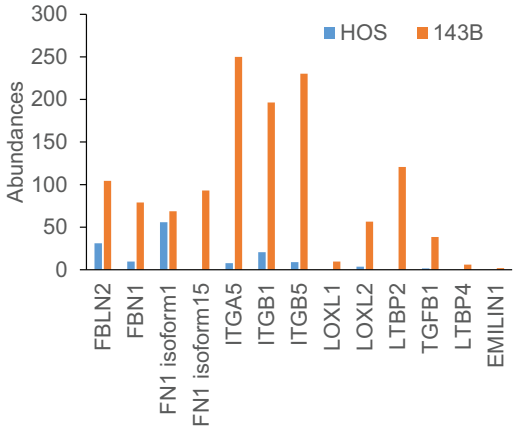

Fig. 7 Abundances of proteins related to the stiffness of 143B exosomes. Protein abundances detected by MS analysis of HOS and 143B cell-derived exosomes. The 143B exosomes contained fibulin 2 (FBLN2), fibrillin-1 (FBN1), fibronectin-1 (FN1), integrin α-5 (ITGA5), integrin β-1 (ITGB1), integrin β-5 (ITGB5), LOXL1, LOXL2, LTBP2, TGFB1, LTBP4, and EMILIN1 at higher levels than HOS exosomes.

Proteomic analysis of exosomes.

To test whether the obtained differences in Young's moduli between HOS and 143B exosomes are associated with differences in their protein content, we performed biochemical characterization. We analyzed exosome proteomes using LC-MS, western blot, and ELISA measurements. The resulting analysis identified a total of 1535 proteins in 143B cell-derived exosomes, and 1464 proteins in HOS cell-derived exosomes. While 272 proteins were included only in 143B exosomes, 201 were unique to HOS exosomes, and 1263 were shared between them (SI, Figure S7a). We extracted 143B or HOS exosomal-specific proteins that were present by over five-fold more in one cell type compared to the other. Overall, 345 and 428 proteins were identified as 143B and HOS exosomal-specific proteins, respectively. These proteins were then subjected to gene ontology (GO) enrichment analysis to determine their molecular and biological functions. The unique biological and molecular functions involved in each exosome are shown in a heatmap (SI, Figure S7b). Proteins specific to elastic fiber formation, including fibulin-2 (FBLN2), fibrillin-1 (FBN1), fibronectin-1 (FN1) with two isoforms, integrin α-5 (ITGA5), integrin β-1 (ITGB1), integrin β-5 (ITGB5), lysyl oxidase enzymes (LOXL1 and LOXL2), latent TGFβ binding protein-2 (LTBP2), LTBP4, TGFβ-1 (TGFB1), and EMILIN1, were identified as being increased in exosomes from the 143B cell line compared with those from HOS cells (Figure 7).

To confirm the existence of these selected proteins in HOS and 143B exosomes, western blotting and ELISA analyses were performed (Figure 8). We confirmed the presence of five proteins

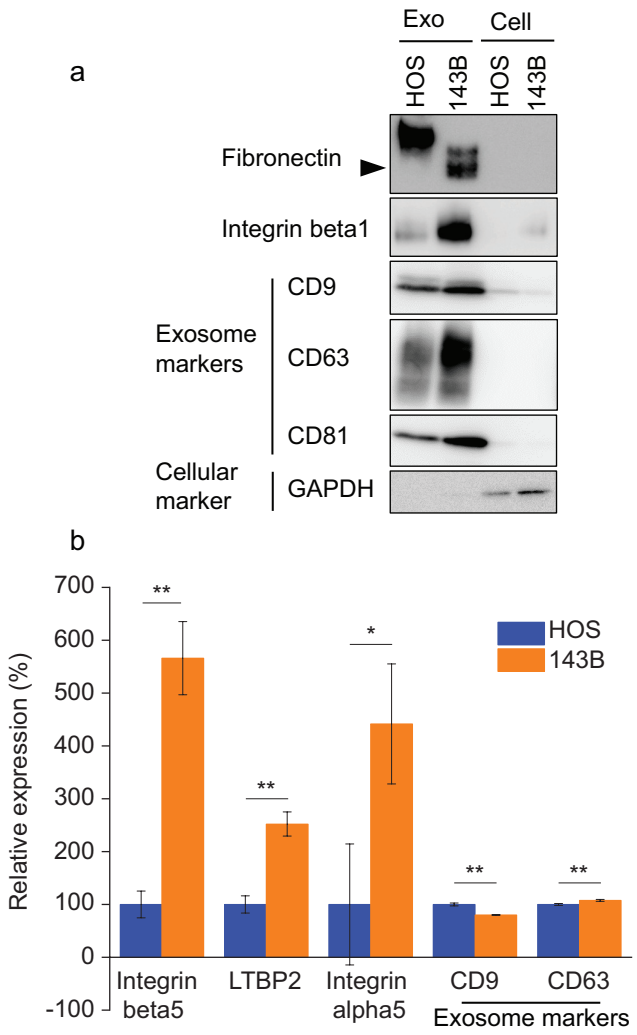

Fig. 8 Protein expression in HOS and 143B cell-derived exosomes. (a) Western blot analysis of fibronectin (FN), integrin β-1 (ITGB1), CD9, CD63, CD81, and glyceraldehyde-3-phosphate dehydrogenase (GAPDH) in 143B and HOS exosomes and their respective parental cells. Exosome lysate or cell lysate were applied at 400 ng/lane and run in 5-20% polyacrylamide gels. The presence of FN, ITGB1, exosomal markers (CD9, CD63, and CD81), and cellular marker (GAPDH) proteins was confirmed for each antibody in the western blot. (b) Expression of some selected proteins in 143B and HOS exosomes obtained via ELISA. HOS and 143B exosomes were attached at 200 ng/well on a TIM4-coated ELISA plate. Integrin β-5 (ITGB5), LTBP2, integrin α-5 (ITGA5), and exosomal markers CD9 and CD63 were detected with each antibody in ELISA analysis. ITGB5, LTBP2, and ITGA5 were found to be highly expressed in 143B cell-derived exosomes compared to HOS cell-derived exosomes. Error bars represent the standard deviation of the mean. Significance level: $P^{*}<0.05$; $P^{**}<0.01$.

previously identified by LC-MS analysis. FN1 and ITGB1 proteins were detected by western blotting in 143B exosomes at higher levels. While ITGB1 was significantly lower in abundance, FN1 was not detectable in exosomes from HOS cells, in agreement with the MS-based proteomic analysis. We note that the parental cells express little ITGB1 or no FN1. This does not mean that the parent cells do not involve FN1 or ITGB1. If the amounts of proteins loaded are increased, FN1 and ITGB1 could also be identified in the cell lysates. However, in this case, it would be difficult to state that FN1 and ITGB1 proteins are selectively sorted onto exosomes or cells.

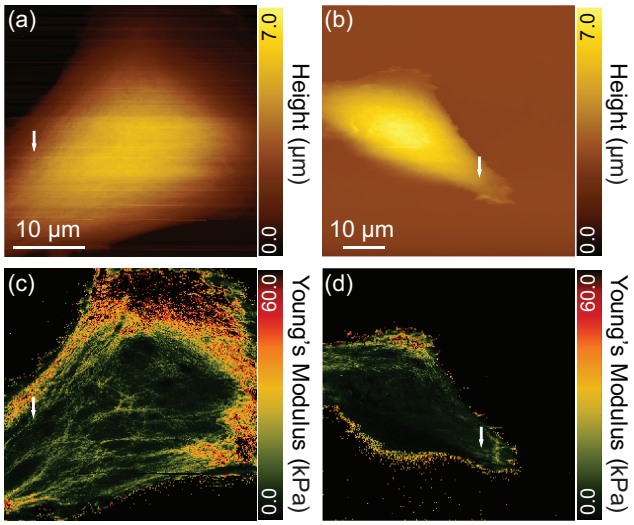

Fig. 9 Mapping the mechanical properties of parental cells that secrete HOS and 143B exosomes. AFM topography image of living HOS (a) and 143B (b) cells seeded on a Petri dish, acquired with a sharp tip in CO_2-independent medium (Leibovitz's L-15) at 37°C. (c-d) Corresponding Young's modulus maps for HOS and 143B cells, respectively. We note that the AFM height images and corresponding Young's modulus maps were recorded with a sharp tip to resolve the subcellular details. Arrows indicate the filamentous structures, probably actin stress fibers. These stiffer subcellular features become apparent when the applied loading force is increased. Note that the regions of increased Young's moduli correspond to the regions with filamentous networks. The density of fibers in HOS cells is higher than that in 143B cells, reflecting the differences in their Young's modulus values.

The expressions of ITGB5, LTBP2, ITGA5, and tetraspanin (CD9 and CD63) proteins within these nanovesicles were determined by ELISA analyses using different antibodies. ITGB5, LTBP2, and ITGA5 were found to be more abundant in 143B cell-derived exosomes compared to HOS cell-derived exosomes, consistent with the LC-MS analyses. These proteins are known to play an essential role in elastic fiber assembly. The main function of elastic fibers is to confer mechanical support to tissues and organs in response to compressive mechanical forces, allowing them to resist mechanical perturbations occurring in their microenvironment[66]. The expression levels of these protein groups greatly influence the rigidity of cells, tissues, and other biostructures. Taken together, our results suggest that the observed higher Young's moduli of the metastatic tumor cell-derived exosomes can be directly linked to the presence of several highly abundant proteins specific to elastic fiber formation.

Mapping the nanomechanical properties of live parental HOS and 143B cells.

The mechanical property differences observed between metastatic and nonmetastatic cancer cell-derived exosomes may be important as biomarkers for assessing the invasive and metastatic potential of tumor cells. It has been well established that tumor cells are generally softer than healthy cells[38,67] and

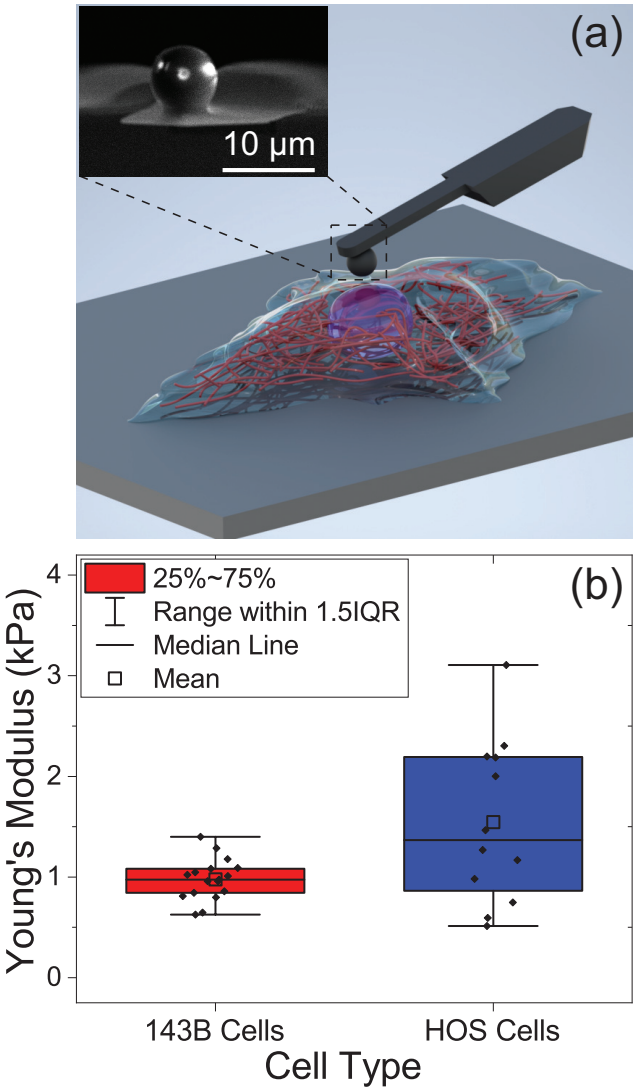

Fig. 10 Comparison of the Young's modulus values for living HOS and 143B cells. (a) Schematic representation of a colloidal probe positioned above the central nuclear region of a cell. Inset image shows a FIB-SEM image of a 7.24-μm spherical silica bead attached to an AFM cantilever. This colloidal probe was employed for all Young's modulus measurements. (b) Box-and-whisker plots of the average Young's modulus values for living HOS and 143B cells seeded on a Petri dish. The Young's modulus measurements were performed in CO_2-independent medium (Leibovitz's L-15) at 37°C. The mean Young's moduli are 1.54 $\pm$ 0.23 kPa and 0.97 $\pm$ 0.05 kPa for HOS and 143B cells, respectively. Each black-filled square indicates the average Young's modulus of an individual cell.

that this is related to their higher invasive potential. We additionally performed biomechanical measurements for the parent cells that secrete 143B- and HOS-exosomes to confirm this. Our results corroborate the general observation that nonmetastatic cells are stiffer than metastatic cells (Figures 9 and 10). The distribution of average Young's moduli of individual live HOS and 143B cells, determined by using a spherical silica bead as an indenter (see Materials and Methods), is displayed as a box-and-whisker plot in Figure 10. The mean Young's moduli of HOS and 143B cells were 1.54 $\pm$ 0.23 kPa and 0.97 $\pm$ 0.05 kPa, respectively. The observed differences in mechanical properties of live HOS and 143B cells are reflected by differences in their cytoskeletal structural organization. A detailed view of the subcellular features of live HOS and 143B cells was provided using a sharp AFM probe (Figure 9). Bundles of fibrous structures, probably actin filaments or stress fibers that become apparent when the applied loading force is increased, were observed over the cell body in both cell lines. However, the nonmetastatic HOS cells showed more actin stress fibers in comparison to their metastatic counterparts (for a more detailed view, see SI, Figures S8 and S9). An entangled networks of these fibrillar structures with increased density might contribute to the higher modulus of HOS cells[68]. The apparent fiber structures were clearly resolved in the Young modulus maps as higher moduli across the cell bodies (Figures 9c and 9d; SI, Figure S9)

Discussion

The significance of exosomes as either potential noninvasive biomarkers for cancer and other diseases or as therapeutic tools has been well recognized in recent years[69]. Their possible use as predictive biomarkers in clinical applications using liquid biopsies strongly demands accurate characterization of their morphological, molecular, and biomechanical properties[70]. However, their small size and structural and compositional heterogeneity make their characterization an extremely challenging task[3]. We employed a high-resolution 3D-AFM-based force mapping method to elucidate the detailed structure and associated nanomechanics of exosomes derived from different cell types, including metastatic and nonmetastatic tumor cells. The 3D-AFM force map enabled us to observe the exosome structural details, which showed distinct local nanodomains that can be associated with the heterogeneous presence of exosomal proteins or genetic material exposed either to the membrane's outer surface or encapsulated within. Furthermore, we found that exosomes derived from the same cell type have diverse morphology in AFM images at the molecular scale (see, Figures 3c; SI, Figure S5b). This morphological variability from a single cell type may arise due to differences in biomolecular contents[28]. The reorganization of membrane proteins on the surface of exosomes dispersed on a solid substrate is also likely to contribute to the observed variable structural features.

We performed AFM nanomechanical measurements to assess exosome biophysical properties, which are closely related to many aspects of vesicle behavior, such as diffusivity, adhesion, shape, vesicle generation, and cellular uptake. Although there were no significant differences in the physical appearance between metastatic and nonmetastatic tumor cell-derived exosomes, their mechanical properties displayed clear differences. An increase in Young's moduli of metastatic tumor cell-derived exosomes was identified compared to those from nonmetastatic tumor cells. Notably, the analyzed modulus data revealed distinct moduli for the different local regions on the exosome surface (SI, Figure S5). This strongly implies high heterogeneity of exosome surfaces for molecular composition, corroborating previous findings[71]. This heterogeneity may also reflect the multifunctional role of exosomes, as different exosome components may function together to activate intercellular signaling.

Our analysis demonstrated that the elastic modulus values for exosomes are within the range reported for nano-sized vesicles comprised of natural membranes[57,59,65], and are relatively high compared to those for synthetic liposomes[49]. The role of lipid and protein composition on the mechanical properties of naturally occurring vesicles has been elucidated by Calò *et al.*[59]. It has been shown that the rigidity of such small natural nanovesicles is determined mainly by their protein content and independent of their lipid composition[59,65]. Vorselen *et al.* compared the bending rigidity of extracellular vesicles from red blood cells taken from healthy and spherocytotic patients[57]. They attributed the observed differences in bending rigidity to differences in protein content. We therefore performed proteomic analysis on exosomes from HOS and 143B cells to identify differentially-expressed proteins. Our results indicated that the metastatic tumor cell-derived exosomes (143B) possessed a significant number of unique proteins related to elastic fiber assembly. The high abundance of this class of proteins in metastatic tumor cell-derived exosomes compared to their nonmetastatic counterparts could be the reason for their increased elastic moduli.

Previously, Sharma *et al.* reported structural and biomolecular differences between normal and tumor-derived saliva exosomes[23] and demonstrated the enrichment of specific proteins present in the membranes of tumor-derived vesicles as determined by a functionalized AFM probe with an antibody specific to the CD63 exosome marker protein. The same group has also reported differences between glioblastoma cell-derived exosomes and normal exosomes[72] and observed the presence of individual nanofilaments extending from the surfaces of the glioblastoma cell-derived exosomes. These nanofilaments are rarely seen in normal exosomes. In addition, Whitehead *et al.* have demonstrated differences between malignant metastatic T24 and malignant nonmetastatic FL3 bladder cell-derived exosomes in terms of their mechanical and exosome-mediated complement activation properties[45]. A recent study has reported the stiffness of subpopulations of exosomes using asymmetric flow field-flow fractionation (AF4)[65]. The authors identified two exosome subpopulations: small exosomes (Exo-S) with a diameter of 60-80 nm and large exosomes (Exo-L) with a diameter of 90-120 nm. These two types of exosomes were found to display distinct stiffness values; Exo-S and Exo-L displayed stiffnesses of approximately 70-420 and 26-73 MPa, respectively. Our results are comparable with the results of Zhang *et al.* for the size and stiffness range found for Exo-S[65].

We performed mechanical property measurements for parental cells that secrete HOS and 143B exosomes. In contrast to their daughter exosomes, the metastatic tumor cells exhibited a lower Young's modulus than their nonmetastatic counterparts. To interpret our results, we performed cell-based ELISA to determine the expression of selected proteins found in daughter exosomes in their parental cells. We found that elastic fiber-associated proteins were highly expressed in HOS cells compared to 143B cells (SI, Figure S10), which is in contrast to their daughter exosomes. Based on these findings, it might be that metastatic tumor cells release exosomes that express increased levels of elastic fiber-associated proteins to preserve their softness. The enhancement of exosome release with specific protein cargoes by tumor cells into their surrounding microenvironment has been reported in several studies, and it can influence tumor growth and metastasis[73].

It can be speculated that although exosomes contain molecular cargoes identical to their cell of origin with different proportions, their Young's moduli are higher than their parent cells. This can be explained by the fact that proteins or other contents involved in exosomal cargoes are confined in a smaller volume forming a tightly packed structure. While the large surface area of the cellular membrane provides a high degree of freedom and softness to the membrane, the exosomes' small size provides a low degree of freedom for the exosomal membrane and higher stiffness. Moreover, an increased internal osmotic pressure of an adherent vesicle might also contribute to the observed higher modulus of exosomes[58]. The change in vesicle volume occurred during the indentation process and due to the adhesive interaction with the underlying substrate, results in an increased outward osmotic pressure. The pressure built up by the spatial confinement of proteins, DNA, and other genetic materials might confer a higher elastic modulus to exosomes compared to their parental cells[74,75].

It is known that tumors are softer than normal tissues[76] and that this softness is associated with malignancy in many tumor types[77,78]. It has been suggested that cell stiffness is due to the F-actin cytoskeleton[79] and extracellular matrix[80], which play important roles in tumor invasion and metastasis. Because they interact with each other via transmembrane protein integrins, their expression and stability affect each other. AFM-based stiffness mapping analysis of biopsies from breast cancer patients have shown uniform stiffness profiles in normal and benign tissues, whereas malignant breast cancer tissues show heterogeneous stiffness profiles with a prominent low-stiffness peak[80]. Analysis of mouse mammary tumor virus-polyoma middle T antigen transgenic mice, a mouse model of breast cancer, show that breast cancer cells with lower stiffness have higher metastatic and invasive abilities[80]. However, an inverse relationship between softness and malignancy has also been reported.

It has been reported that exosomes expressing functional fibronectin on their surfaces are secreted not only from nontumor cells[81] but also from tumor cells. Moon *et al.* reported that a larger number of fibronectin-expressing extracellular vesicles were detected in the plasma of breast cancer patients than in disease-free individuals and in breast cancer patients after surgical resection[82]. In terms of functional analysis, fibronectin-expressing exosomes from human fibrosarcoma have the ability to control directional cell movement[83], and fibronectin-expressing exosomes from human myeloma promote tumor growth and invasion by activating the MAPK pathway in receiver cells[84]. Our data show that exosomes from highly aggressive OS cells express elastic fiber-related proteins, including fibronectin and fibrillin, at higher levels than those from nonaggressive OS cells, and that the higher expression of elastic fiber-related proteins causes higher exosome stiffness. These results are consistent with previous reports.

It is well known that mutant K-RAS alters exosomes qualita-

tively and quantitatively[85,86]. Our data also show an increase in the amount of elastic fiber-related proteins per exosome particle. The synergistic effects of increased exosome secretion and selective protein sorting may be responsible for the decrease in elastic fiber-related proteins on the surfaces of 143B cells, which causes a decrease in cell stiffness. Elastic fibers have reciprocal effects: a reduction in cellular mobility due to mechanical stiffness in cells, and the activation of cellular mobility and proliferation by signal transduction via exosomes. These reciprocal effects on tumor pathogenesis may result in a disparate relationship between cell stiffness and tumor malignancy. A similar phenomenon may occur in many types of tumors, as increased exosome secretion and the alteration of exosomal cargo proteins is well known, especially in Src-expressing tumors[87].

Conclusions

We applied 3D-AFM, in force mapping mode, to assess the structural and nanomechanical properties of exosomes released from three types of cells in a physiologically relevant environment. The 3D-AFM force maps enabled previously unidentified substructures of individual exosomes to be observed, indicating the presence of distinct nanodomains bulging out from the membrane surface. These protruding features were attributed to membrane-associated proteins exposed on the outer surface. To determine the identity of these features, tip functionalization with antibodies specific to exosomal surface proteins[88] is necessary. This will be our next goal. The nanomechanical properties of exosomes were determined from the 3D-force maps using the Sneddon (conical) model. A relatively high Young's modulus value, ranging from 50 to 350 MPa on average, was found compared to that of synthetic liposomes[48,49], which signifies a crucial role for membrane-associated proteins in exosome mechanical properties. We revealed malignancy state-dependent changes in the mechanical properties of exosomes and their parent cells, and our results showed differences between the nanomechanical properties of metastatic and nonmetastatic tumor cell-derived exosomes. Highly aggressive metastatic 143B cell-derived exosomes exhibited an increased Young's modulus, 192 MPa, compared with 118 MPa for nonmetastatic HOS cell-derived exosomes. Protein profiling analysis using LC-MS/MS, western blotting, and ELISA indicated that the metastatic tumor cell-derived exosomes were enriched in specific proteins involved in the elastic fiber formation. We thus concluded that these elastic fiber-associated proteins were responsible for the increased vesicle rigidity. We also performed nanomechanical measurements for parental HOS and 143B cells that secreted the exosomes to confirm the general principle that malignant cells tend to be softer than their healthy counterparts. The metastatic tumor cells (143B) had an apparent Young's modulus lower than that of the nonmetastatic ones (HOS). In contrast to their daughter exosomes, cell-based ELISA analysis indicated that the elastic fiber-associated proteins are expressed at significantly higher levels in parental HOS cells than in 143B cells. Based on these findings, it is plausible that metastatic tumor cells may exploit exosomes to release stiffening proteins to preserve their softness.

Characterizing exosome structural and biomechanical properties with high spatial resolution can provide useful information for their possible use as drug delivery systems and improve our understanding of the mechanisms of exosome-mediated cell-surface interactions and cellular functions. Our results suggest that exosome stiffness combined with their easy accessibility in almost all bodily fluids gives them the potential to serve as noninvasive biomarkers for early-stage identification of changes induced by the presence of tumors and other diseases. Further studies are underway to explore the stiffness characteristics of exosomes derived from other types of cells to identify the possible changes related to tumors and other diseases.

Methods

Experimental Details

Cell culture and exosome isolation

The murine OS cell line, LM8, was obtained from RIKEN BRC (Ibaraki, Japan). The human nonaggressive OS cell line expressing wild-type k-ras, HOS, and the highly aggressive k-ras-activated OS cell line, 143B (Ref.[47]), were obtained from ATCC (Manassas, VA, USA). To isolate exosomes, these cells were cultured in Advanced DMEM (Thermo Fisher Scientific, Waltham, MA, USA) with penicillin, streptomycin, L-glutamine, and 2% exosome-depleted fetal bovine serum (FBS, Bio-West, NuaillÃ©, France). The exosomes were depleted from FBS by centrifuging a mixture of one volume of heat-inactivated FBS and a 1/5 volume of 50% polyethylene glycol 10,000 at 1,500 $\times$ g for 30 min, and the exosome-depleted FBS was recovered in the supernatant[89]. Conditioned medium of these cells was centrifuged at 300 $\times$ g, 4°C for 5 min, 2,000 $\times$ g, 4°C for 20 min, and 10,000 $\times$ g, 4°C for 30 min to remove dead cells, cellular debris, and large extracellular vesicles, respectively, and the supernatant containing exosomes was collected. Exosomes were isolated from the supernatant by using MagCapture^{TM} Exosome Isolation Kit PS (Fujifilm Wako Pure Chemical Corporation, Osaka, Japan) (Ref.[50]) according to the product's protocol. Concentrations and sizes of the isolated exosomes were determined by a nanoparticle tracking analyzer using NanoSIGHT^{TM} LM10 (Malvern Panalytical, Malvern, UK). Protein concentrations of the exosomes were determined using Pierce^{TM} BCA Protein Assay Kit (Thermo Fisher Scientific). The highly purified exosomes were stored at 4°C for several days, or −20°C for a few months for further use.

Protein identification using nano-liquid chromatography mass spectrometry (LC-MS)

The isolated exosomes from HOS or 143 cells were lysed in 125 μl of RIPA buffer [0.1% sodium dodecyl sulfate, 0.5% sodium deoxycholate, 1% Triton X-100, 150 mM NaCl, 2 mM EDTA, 50 mM Tris-HCl (pH 8.0)]. Proteins were recovered from the lysate by chloroform-methanol precipitation. In brief, the lysate was mixed with 500 μl of methanol and 125 μl of chloroform, and centrifuged at 15,000 $\times$ g, 4° for 1 min. The lower phase was transferred to a new tube containing 500 μl of methanol, centrifuged at 15,000 $\times$ g, 4° for 2 min, and then the pellets were resuspended in 6 M urea and 50 mM TEAB (pH 8.5). Proteins were reduced with 5 mM TCEP at 37° for 30 min, alkylated with 24

mM iodoacetamide at 25° for 30 min, and digested with trypsin (Promega, Madison, WI, US) at a 1:10 enzyme/protein ratio at 37° for 16 h. Peptides were desalted with Stage tip (Thermo Fisher Scientific) and recovered in 5% ACN containing 0.1% trifluoroacetic acid. The trypsin-digested peptides were loaded onto an EASY-nLC 1200 (Thermo Fisher Scientific) equipped with an Acclaim PepMap 100 C18 LC column (Thermo Fisher Scientific), equilibrated with 0.1% formic acid, and eluted with a linear acetonitrile gradient from 0 to 35% in 0.1% formic acid. The eluted peptides were loaded and separated on a NANO-HPLC capillary column C18 (Nikkyo Technos, Tokyo, Japan) at 2 kV of spray voltage and 275° of ion transfer tube temperature. The peptide ions were detected using Orbitrap QE plus MS (Thermo Fisher Scientific). To identify proteins, MS/MS search and label-free quantification were carried out using Proteome Discoverer (PD) 2.2 (Thermo Fisher Scientific) with SEQUEST HT search algorithms against the *Homo sapiens* protein database (Swiss-Prot, Tax ID 9609). Normalization of the abundances was performed using total peptide amount mode. Proteins contained at more than 5-fold higher abundances in HOS or 143B exosomes were classified as HOS- or 143B-specific exosomal proteins. They were performed in an enriched ontology analysis using Metascape software[90].

Western blot analysis

Cells at subconfluency in 60-mm dish were washed with PBS(-) and lysed in RIPA buffer with protease inhibitor cocktail (FUJIFILM Wako Pure Chemical Corporation) on ice for 20 min. The lysed cells were centrifuged at 14,000 $\times$ g, 4°C for 20 min to collect the cellular lysates. Protein concentrations were determined with a Pierce™ BCA Protein Assay Kit (Thermo Fisher Scientific). The cellular lysates or the isolated exosomes were prepared in sample buffer [2% SDS, 10% glycerol, 0.01% bromophenol blue, 50 mM Tris-HCl (pH 6.8)]. They were then run on a SuperSep™ Ace, 5-20% gel (FUJIFILM Wako Pure Chemical Corporation) at 200 V for 60 min, followed by transfer to a polyvinylidene fluoride membrane (Bio-Rad Laboratories, Hercules, CA, USA). The membrane was blocked in PBS containing 5% skim milk (Megmilk Snow Brand, Tokyo, Japan) and 0.05% Tween 20 for 1 h, and subsequently treated with each diluted primary antibody for 2 h, then each diluted HRP-conjugated secondary antibody for 1 h. The proteins were detected using Luminata™ Forte Western HRP Substrate (Merck, Darmstadt, Germany) and an ImageQuant LAS4000 Mini (GE Healthcare, Chicago, IL, USA). Anti-fibronectin antibody (clone FN-3, Thermo Fisher Scientific), anti-human integrin β1 antibody (clone TS2/16, BioLegend, San Diego, CA, USA), anti-human CD9 antibody (clone HI9a, BioLegend), anti-human CD63 antibody (clone H5C6, BioLegend), human CD81 antibody (clone 5A6, BioLegend), and anti-GAPDH antibody (clone 3H12, Medical & Biological Laboratories, Aichi, Japan) were used as the primary antibodies. HRP-conjugated anti-mouse IgG (Jackson ImmunoResearch, West Grove, PA, USA) was used as the secondary antibody.

Exosome-Enzyme-Linked Immuno-sorbent Assay (Exosome-ELISA)

The isolated exosomes from HOS or 143B cells were prepared at 200 ng/100 μl in Tris-buffered saline (TBS) containing 1% BSA and 2 mM $CaCl_2$, and subjected to ELISA, following a similar method described previously[89]. Recombinant TIM4-Fc protein (FUJIFILM Wako Pure Chemical Corporation) was immobilized at 100 ng/100 μl in 100 mM bicarbonate/carbonate buffer (pH 9.6) overnight at 4°C in ELISA 96-well plates (AGC Techno Glass, Shizuoka, Japan). The wells were blocked with TBS containing 1% BSA and 0.05% Tween 20 for 1 h. The isolated exosomes were bound to TIM4-Fc for 2 h. The wells were treated with each primary antibody for 1.5 h and subsequently treated with an HRP-conjugated secondary antibody for 1 h. HRP activity was detected using the ELISA POD Substrate TMB Kit (Nacalai Tesque, Kyoto, Japan). Antibodies against integrin β (clone KN52, Thermo Fisher Scientific), LTBP2 (polyclonal antibody HPA003415, Merck), integrin α 5 (clone P1D6, BioLegend), human CD9 (clone HI9a, BioLegend), and CD63(clone H5C6, BioLegend) were used as the primary antibodies. HRP-conjugated anti-mouse IgG (Jackson ImmunoResearch) and HRP-conjugated anti-rabbit IgG (Jackson ImmunoResearch) were used as the secondary antibodies.

Cell-based ELISA

HOS or 143B cells were seeded in Advanced DMEM-2%FBS at 50% confluency on a 96-well plate and cultured for 24 h. The cells were washed twice with PBS(-) and fixed with 4% paraformaldehyde at room temperature for 15 min. After washing with PBS(-), the fixed cells were blocked in PBS(-) containing 1% BSA and 0.05% Tween 20 for 2 h. The cells were treated with each primary antibody at 4°C overnight and subsequently treated with an HRP-conjugated secondary antibody at 4°C for 2 h. HRP activity was detected using the ELISA POD Substrate TMB Kit. Antibodies used in this experiment were the same as those used in the Exosome-ELISA.

Sample preparation, mica functionalization, and imaging in a fluid

The purified exosomes—known to display a negative zeta potential—were immobilized on an APTES (Tokyo Chemical Industry)-modified mica substrate for AFM observations. Briefly, after pumping out of a vacuum desiccator for about 5 min, 30 μL of APTES solution was placed in an open glass container located at the bottom of a clean desiccator. Following this process, the freshly cleaved mica substrate was exposed to APTES vapors for about 15 min. After removing the APTES solution, the desiccator was purged, and the APTES-functionalized mica substrate was stored inside overnight. After the mica disc was removed from the desiccator, a 100 μL drop of each isolated vesicle solution was immediately spotted onto the APTES-modified mica substrate and left to adsorb for 15 min at room temperature. The surface was then rinsed thoroughly either with TBS buffer or Milli-Q water several times to remove excess unbound vesicles, and then the vesicles were subjected to AFM investigation and force mapping

under Milli-Q water.

In this preparation step, exosomes were found to bind tightly enough on the APTES-modified mica surface by electrostatic interactions to be appropriately observed by AFM in a liquid environment without much influence on the measured size of vesicles, as determined by their cross-sectional profiles. We note that strong silanization of the mica substrate by APTES can lead to a rupture of spherical vesicles, resulting in the formation of flattened-bilayer patches with an average thickness of 4.5–5 nm, the release of genetic material, and adsorption onto the substrate (see SI, Figure S3). All AFM data were taken at room temperature and under buffer conditions of Milli-Q water with a conductivity of < 18.2 MΩcm.

FM-AFM setup

Structural and mechanical characterization of exosomes was performed with a home-made frequency modulation AFM (FM-AFM) system operating in a liquid environment equipped with an ultra-low noise cantilever deflection sensor[91,92]. A photothermal excitation technique was used to drive the cantilever oscillation[93]. AFM scanning was controlled by a commercial SPM controller (ARC2, Asylum Research), and the oscillation amplitude of the cantilever was kept constant using a commercially available controller (OC4, SPECS). The AFM was operated in constant frequency shift ($\Delta f(z)$) mode, where the tip-sample distance was adjusted such that $\Delta f(z)$ was kept constant. The AFM data were acquired using two types of commercially available AFM cantilevers (AC240 and 240AC-NG, purchased from Olympus and OPUS, respectively) with nominal spring constants of 2 N/m and nominal tip radii of $<$7 nm. The AFM tips used have pyramidal shapes with a half-opening angle of 18°. After each measurement, the spring constant of the cantilevers was experimentally determined using the thermal noise method to quantify the mechanical properties of the exosomes[94]. The obtained AFM images were rendered using WSXM or Gwyddion software.

3D-AFM force mapping of exosomes

The 3D force maps of exosomes were realized by the 3D-AFM method developed by Fukuma *et al.*[95]. An overview AFM topography image of the surface was first acquired to locate individual exosomes. The selected vesicle was then imaged at a higher resolution to perform the 3D-force mapping experiment. A 3D-frequency shift (Δf) map covering an area of 100-200 $\times$ 100-200 nm square—divided into grids of 128 $\times$ 128 pixels—was acquired by recording the Δf for each pixel on the sample surface. A 3D Δf map was produced by recording in real time the $\Delta f(z)$ with respect to the tip positions in the 3D interfacial space. During the 3D Δf mapping, the averaged tip-sample distance was modulated such that the averaged Δf became constant. The acquired 3D Δf map was converted to a 3D force map using Sader's algorithm[96]. We note that for a stable imaging and force mapping process, in some cases, we used the dissipation channel as a feedback signal to regulate tip-sample separations. Details of the 3D-AFM force mapping and data evolution processes can be found in Ref.[95].

Nanomechanical mapping of exosomes

The 3D-force data processing and the extraction of Young's modulus values were performed using home-build Labview based software. The developed program can fit the force-distance curves at each pixel in the 3D dataset with appropriate contact mechanical models that include different tip geometries and can acquire Young's modulus maps. The approaching parts of the force-distance curves were used for the Young's modulus analysis. The baseline correction, including the flattening of the inclination of force-distance curves and aligning at zero force value, was initially performed for a region far from the surface. Then the contact point was determined. The contact point determination and force curve fitting can be done automatically or manually. After automatic calculations, all force curves were checked manually to avoid any poorly fitted data points that could cause incorrect elasticity values. The Young's modulus can be determined from the contact point to a given indentation distance set by the user. It is known that at a high loading force or larger indentation, the substrate starts to play a role in the mechanical properties[97,98]. Therefore, we limited the indentation distances on the order of vesicle membrane thickness, thus allowing us to probe the mechanical properties in the elastic regime. We constructed the resulting Young's modulus histogram from the central region of an individual vesicle covering an area typically 30 $\times$ 30 nm^2 with 64 $\times$ 64 pixels to minimize the well-known substrate stiffening effects. We calculated Young's modulus based on the following equation (Eq. 1) developed for conical indenters:

$$F = \frac{2 \times \tan(\alpha) \times E \times \delta^2}{\pi(1-\nu^2)} \quad (1)$$

Where F is the applied loading force, E is Young's modulus, ν is Poisson's ratio of a sample, and α is the half-opening angle of the cone. Poisson's ratio was assumed to be constant and taken as 0.5, which is typical for soft biomaterials. The mean value of Young's modulus distribution for each vesicle was obtained by fitting the Gaussian distribution to the histogram constructed from the 4096 force-distance curves. The results are reported as the mean $\pm$ standard deviation.

Nanomechanical mapping of cell surfaces

All AFM measurements for the cell mechanical characterization were conducted using a Nanowizard-III AFM system (JPK Instruments AG, Berlin, Germany) equipped with an inverted optical microscope (Eclipse Ti2-E, Nikon), enabling precise positioning of the cantilever on the cell. AFM imaging and elasticity measurements of live cells seeded on a Petri dish were performed in CO_2-independent medium (Leibovitz's L-15) at 37°C using a JPK Petri Dish Heater. The elastic moduli of HOS and 143B cells were obtained with a well-defined nano-probe fabricated by gluing a spherical silica bead (with a diameter of 7.24 μm) to the end of a BL-AC40TS-C2 Biolever mini cantilever (Olympus, Japan) with a biocompatible, two-component epoxy (EPO-TEK 353ND). This has the advantage of preventing the effects of cell inhomogeneities that appear at a small scale. The spring constant of the AFM indenter was determined to be 0.126 N/m, using the ther-

mal noise spectra before each experiment[94]. After the attachment of the silica bead, we found that the resonance frequency and spring constant of the cantilever remained nearly the same as the AC40 cantilever. To visualize the subcellular features, we used a commercially available Biolever mini BL-AC40TS-C2 cantilever with a nominal tip radius of < 8 nm and spring constant of ≈ 0.09 N/m.

We used the advanced QI mode operation of the JPK system to acquire mechanical property maps of the cells. First, the AFM colloidal probe was precisely positioned over the top of the central nuclear region of a freshly prepared living cell to reduce the underlying substrate's effects on the Young's modulus measurements. The force maps were then recorded over a scan area of 10 $\times$ 10 μm^2 located on the nuclear region of a cell (including 64 $\times$ 64 pixels, i.e., 4096 individual force-distance curves). A peak force set-point of 1.5 nN was applied for all force maps. For this particular loading force, the average indentation depth was found to be in a range of 400 to 800 nm depending on the location on the cell surfaces. This range of indentations was previously suggested for the proper determination of the contact point[99]. As exemplified in Figure S9, this indentation range is large enough to reach a plateau region where the Young's modulus value is independent of the indentation depth, which is a prerequisite for accurate elastic modulus measurements. The individual force-distance curves were acquired with a constant loading rate of 15 μm/s and a data sample rate of 3 kHz, which corresponds to 800 $\times$ 800 pixels. The vertical z-ramp range was set at 5 μm for all measurements. The Young's moduli of cells were determined by fitting the approach segment of a force-indentation curve to a Hertzian/Sneddon model modified for a spherical colloidal probe[60]. The mean values of the Young's moduli were determined by applying a Gaussian fitting to the Young's modulus histogram obtained for each cell. We consistently used the same colloidal probe (with 7.24 μm diameter) for all Young's modulus measurements with identical acquisition settings so that the Young's modulus values could be directly compared. The Poisson's ratio of the cells was assumed to be constant, with a value of 0.5. The image processing and Young's modulus data analysis were performed with JPK Data Processing software.

Author contributions

A.Y., T.Y., T.F., and R.H. conceived and planned the experiments. A.Y. performed the AFM experiments and analyzed the data. T.Y. and Y.A. isolated exosomes from cell cultures and performed MS, western blotting, and ELISA analysis. A.B. helped perform the cell measurements. A.Y. wrote the manuscript with input from all authors. All authors reviewed the manuscript.

Conflicts of interest

The authors declare no competing financial interest.

Acknowledgements

This work was supported by Grants-in-Aid for Scientific Research (No. 20H00345 and No. 20K05321) from the Ministry of Education, Culture, Sports, Science, and Technology of Japan (MEXT). This work was also supported in part by a fund from Core Research Evolutionary Science and Technology (CREST) of the Japan Science and Technology Agency (JST) (No. JPMJCR18H4 (R.H.)). This work was also partly funded by JST-Mirai Program (No. 18077272). The authors thank the World Premier International Research Center Initiative (WPI); MEXT, Japan; and the Kanazawa University Fund (Strategic Research Promotion Program, Core-to-Core Program). The authors also acknowledge financial support from the Sumitomo Foundation (No. 190382). We thank W. Weilin and I. Hirokazu for their technical support.

Notes and references

1 P. D. Robbins and A. E. Morelli, *Nature Reviews Immunology*, 2014, **14**, 195–208.
2 C. Sheridan, *Nature Biotechnology*, 2016, **34**, 359–360.
3 R. Kalluri and V. S. LeBleu, *Science*, 2020, **367**, eaau6977.
4 A.-K. Ludwig and B. Giebel, *The International Journal of Biochemistry & Cell Biology*, 2012, **44**, 11–15.
5 C. Bang and T. Thum, *The International Journal of Biochemistry and Cell Biology*, 2012, **44**, 2060–2064.
6 G. van Niel, I. Porto-Carreiro, S. Simoes and G. Raposo, *The Journal of Biochemistry*, 2006, **140**, 13–21.
7 S. Mathivanan, C. J. Fahner, G. E. Reid and R. J. Simpson, *Nucleic Acids Research*, 2012, **40**, D1241–D1244.
8 R. M. Johnstone, M. Adam, J. R. Hammond, L. Orr and C. Turbide, *Journal of Biological Chemistry*, 1987, **262**, 9412–9420.
9 S. Mathivanan, H. Ji and R. J. Simpson, *Journal of Proteomics*, 2010, **73**, 1907–1920.
10 M. Mathieu, L. Martin-Jaular, G. Lavieu and C. Théry, *Nature Cell Biology*, 2019, **21**, 9–17.
11 J. Skog, T. Würdinger, S. van Rijn, D. H. Meijer, L. Gainche, W. T. Curry, B. S. Carter, A. M. Krichevsky and X. O. Breakefield, *Nature Cell Biology*, 2008, **10**, 1470–1476.
12 W. Li, C. Li, T. Zhou, X. Liu, X. Liu, X. Li and D. Chen, *Molecular Cancer*, 2017, **16**, 145.
13 S. A. Melo, L. B. Luecke, C. Kahlert, A. F. Fernandez, S. T. Gammon, J. Kaye, V. S. LeBleu, E. A. Mittendorf, J. Weitz, N. Rahbari, C. Reissfelder, C. Pilarsky, M. F. Fraga, D. Piwnica-Worms and R. Kalluri, *Nature*, 2015, **523**, 177–182.
14 M. Madeo, P. L. Colbert, D. W. Vermeer, C. T. Lucido, J. T. Cain, E. G. Vichaya, A. J. Grossberg, D. Muirhead, A. P. Rickel, Z. Hong, J. Zhao, J. M. Weimer, W. C. Spanos, J. H. Lee, R. Dantzer and P. D. Vermeer, *Nature Communications*, 2018, **9**, 4284.
15 V. P. Jayaseelan, *Cancer Gene Therapy*, 2020, **27**, 395–398.
16 M. Nawaz, G. Camussi, H. Valadi, I. Nazarenko, K. Ekström, X. Wang, S. Principe, N. Shah, N. M. Ashraf, F. Fatima, L. Neder and T. Kislinger, *Nature Reviews Urology*, 2014, **11**, 688–701.
17 A. Becker, B. K. Thakur, J. M. Weiss, H. S. Kim, H. Peinado and D. Lyden, *Cancer Cell*, 2016, **30**, 836–848.
18 H.-G. Zhang and W. E. Grizzle, *The American Journal of Pathology*, 2014, **184**, 28–41.
19 S. Keerthikumar, D. Chisanga, D. Ariyaratne, H. A. Saffar, S. Anand, K. Zhao, M. Samuel, M. Pathan, M. Jois, N. Chil-

amkurti, L. Gangoda and S. Mathivanan, *Journal of Molecular Biology*, 2016, **428**, 688–692.

20 D.-S. Choi, D.-K. Kim, Y.-K. Kim and Y. S. Gho, *Mass Spectrometry Reviews*, 2015, **34**, 474–490.

21 H. Valadi, K. Ekström, A. Bossios, M. Sjöstr and, J. J. Lee and J. O. Lötvall, *Nature Cell Biology*, 2007, **9**, 654–659.

22 A. Zlotogorski-Hurvitz, D. Dayan, G. Chaushu, T. Salo and M. Vered, *Journal of Cancer Research and Clinical Oncology*, 2016, **142**, 101–110.

23 S. Sharma, B. M. Gillespie, V. Palanisamy and J. K. Gimzewski, *Langmuir*, 2011, **27**, 14394–14400.

24 D. D. Taylor, K. S. Lyons and Çiçek Gerçel-Taylor, *Gynecologic Oncology*, 2002, **84**, 443–448.

25 C. Théry, M. Ostrowski and E. Segura, *Nature Reviews Immunology*, 2009, **9**, 581–593.

26 X. Zhang, X. Yuan, H. Shi, L. Wu, H. Qian and W. Xu, *Journal of Hematology & Oncology*, 2015, **8**, 83.

27 E. Crowley, F. Di Nicolantonio, F. Loupakis and A. Bardelli, *Nature Reviews Clinical Oncology*, 2013, **10**, 472–484.

28 D. Zabeo, A. Cvjetkovic, C. Lässer, M. Schorb, J. Lötvall and J. L. Höög, *Journal of Extracellular Vesicles*, 2017, **6**, 1329476.

29 B. György, T. G. Szabó, M. Pásztói, Z. Pál, B. Misják, Petraand Aradi, V. László, É. Pállinger, E. Pap, Á. Kittel, G. Nagy, A. Falus and E. I. Buzás, *Cellular and Molecular Life Sciences*, 2011, **68**, 2667–2688.

30 S. Sharma, H. I. Rasool, V. Palanisamy, C. Mathisen, M. Schmidt, D. T. Wong and J. K. Gimzewski, *ACS Nano*, 2010, **4**, 1921–1926.

31 E. Pol, F. A. W. Coumans, A. E. Grootemaat, C. Gardiner, I. L. Sargent, P. Harrison, A. Sturk, T. G. Leeuwen and R. Nieuwland, *Journal of Thrombosis and Haemostasis*, 2014, **12**, 1182–1192.

32 C. Théry, S. Amigorena, G. Raposo and A. Clayton, *Current Protocols in Cell Biology*, 2006, **30**, 3.22.1–3.22.29.

33 J. Wang, Y. Yao, J. Wu and G. Li, *Int J Clin Exp Pathol*, 2015, **8**, 6135–6142.

34 Y. Yuana, R. I. Koning, M. E. Kuil, P. C. N. Rensen, A. J. Koster, R. M. Bertina and S. Osanto, *Journal of Extracellular Vesicles*, 2013, **2**, 21494.

35 D. L. Rupert, V. Claudio, C. Lässer and M. Bally, *Biochimica et Biophysica Acta (BBA) - General Subjects*, 2017, **1861**, 3164–3179.

36 H. Shao, J. Chung, L. Balaj, A. Charest, D. D. Bigner, B. S. Carter, F. H. Hochberg, X. O. Breakefield, R. Weissleder and H. Lee, *Nature Medicine*, 2012, **18**, 1835–1840.

37 Y. F. Dufrêne, T. Ando, R. Garcia, D. Alsteens, D. Martinez-Martin, A. Engel, C. Gerber and D. J. Müller, *Nature Nanotechnology*, 2017, **12**, 295–307.

38 S. E. Cross, Y.-S. Jin, J. Rao and J. K. Gimzewski, *Nature Nanotechnology*, 2007, **2**, 780–783.

39 N. Mandriota, C. Friedsam, J. A. Jones-Molina, K. V. Tatem, D. E. Ingber and O. Sahin, *Nature Materials*, 2019, **18**, 1071–1077.

40 M. Krieg, G. Fläschner, D. Alsteens, B. M. Gaub, W. H. Roos, G. J. L. Wuite, H. E. Gaub, C. Gerber, Y. F. Dufrêne and D. J. Müller, *Nature Reviews Physics*, 2019, **1**, 41–57.

41 D. Vorselen, W. H. Roos, J. J. van Loon and G. J. Wuite, *Biophysical Journal*, 2013, **104**, 620a.

42 P. Parisse, I. Rago, L. Ulloa Severino, F. Perissinotto, E. Ambrosetti, P. Paoletti, M. Ricci, A. P. Beltrami, D. Cesselli and L. Casalis, *European Biophysics Journal*, 2017, **46**, 813–820.

43 J. Woo, S. Sharma and J. Gimzewski, *Journal of Circulating Biomarkers*, 2016, **5**, 11.

44 H. Choi and J. Mun, *Applied Microscopy*, 2017, **47**, 171–175.

45 B. Whitehead, L. Wu, M. L. Hvam, H. Aslan, M. Dong, L. Dyrskjøt, M. S. Ostenfeld, S. M. Moghimi and K. A. Howard, *Journal of Extracellular Vesicles*, 2015, **4**, 29685.

46 R. Garimella, L. Washington, J. Isaacson, J. Vallejo, M. Spence, O. Tawfik, P. Rowe, M. Brotto and R. Perez, *Translational Oncology*, 2014, **7**, 331–340.

47 H. H. Luu, Q. Kang, J. K. Park, W. Si, Q. Luo, W. Jiang, H. Yin, A. G. Montag, M. A. Simon, T. D. Peabody, R. C. Haydon, C. W. Rinker-Schaeffer and T.-C. He, *Clinical & Experimental Metastasis*, 2005, **22**, 319–329.

48 S. Li, F. Eghiaian, C. Sieben, A. Herrmann and I. A. Schaap, *Biophysical Journal*, 2011, **100**, 637–645.

49 N. Delorme and A. Fery, *Phys. Rev. E*, 2006, **74**, 030901.

50 W. Nakai, T. Yoshida, D. Diez, Y. Miyatake, T. Nishibu, N. Imawaka, K. Naruse, Y. Sadamura and R. Hanayama, *Scientific Reports*, 2016, **6**, 33935.

51 M. Miyanishi, K. Tada, M. Koike, Y. Uchiyama, T. Kitamura and S. Nagata, *Nature*, 2007, **450**, 435–439.

52 E. Hosseini-Beheshti, S. Pham, H. Adomat, N. Li and E. Tomlinson Guns, *Molecular & cellular proteomics : MCP*, 2012, **11**, 863–85.

53 A. Bobrie, M. Colombo, S. Krumeich, G. Raposo and C. Thery, *Journal of Extracellular Vesicles*, 2012, **1**, 18397.

54 H. Asakawa, S. Yoshioka, K.-i. Nishimura and T. Fukuma, *ACS Nano*, 2012, **6**, 9013–9020.

55 B. J. Albers, T. C. Schwendemann, M. Z. Baykara, N. Pilet, M. Liebmann, E. I. Altman and U. D. Schwarz, *Nature Nanotechnology*, 2009, **4**, 307–310.

56 T. Fukuma, *Science and Technology of Advanced Materials*, 2010, **11**, 033003.

57 D. Vorselen, S. M. van Dommelen, R. Sorkin, M. C. Piontek, J. Schiller, S. T. Döpp, S. A. A. Kooijmans, B. A. van Oirschot, B. A. Versluijs, M. B. Bierings, R. van Wijk, R. M. Schiffelers, G. J. L. Wuite and W. H. Roos, *Nature Communications*, 2018, **9**, 4960.

58 D. Vorselen, F. C. MacKintosh, W. H. Roos and G. J. Wuite, *ACS Nano*, 2017, **11**, 2628–2636.

59 A. Calò, D. Reguera, G. Oncins, M.-A. Persuy, G. Sanz, S. Lobasso, A. Corcelli, E. Pajot-Augy and G. Gomila, *Nanoscale*, 2014, **6**, 2275–2285.

60 I. N. Sneddon, *International Journal of Engineering Science*, 1965, **3**, 47–57.

61 X. Liang, G. Mao and K. Ng, *Journal of Colloid and Interface Science*, 2004, **278**, 53–62.

62 D. E. Laney, R. A. Garcia, S. M. Parsons and H. G. Hansma, *Biophysical Journal*, 1997, **72**, 806–813.

63 X. Liang, G. Mao and K. S. Ng, *Colloids and Surfaces B: Biointerfaces*, 2004, **34**, 41–51.

64 E. Willms, H. J. Johansson, I. Mäger, Y. Lee, K. E. M. Blomberg, M. Sadik, A. Alaarg, C. E. Smith, J. Lehtiö, S. EL Andaloussi, M. J. Wood and P. Vader, *Scientific Reports*, 2016, **6**, 22519.

65 H. Zhang, D. Freitas, H. S. Kim, K. Fabijanic, Z. Li, H. Chen, M. T. Mark, H. Molina, A. B. Martin, L. Bojmar, J. Fang, S. Rampersaud, A. Hoshino, I. Matei, C. M. Kenific, M. Nakajima, A. P. Mutvei, P. Sansone, W. Buehring, H. Wang, J. P. Jimenez, L. Cohen-Gould, N. Paknejad, M. Brendel, K. Manova-Todorova, A. Magalhães, J. A. Ferreira, H. Osório, A. M. Silva, A. Massey, J. R. Cubillos-Ruiz, G. Galletti, P. Giannakakou, A. M. Cuervo, J. Blenis, R. Schwartz, M. S. Brady, H. Peinado, J. Bromberg, H. Matsui, C. A. Reis and D. Lyden, *Nature Cell Biology*, 2018, **20**, 332–343.

66 C. M. Kielty, M. J. Sherratt and C. A. Shuttleworth, *Journal of Cell Science*, 2002, **115**, 2817–2828.

67 M. Lekka and P. Laidler, *Nature Nanotechnology*, 2009, **4**, 72–72.

68 C. Rotsch and M. Radmacher, *Biophysical Journal*, 2000, **78**, 520–535.

69 R. Xu, A. Rai, M. Chen, W. Suwakulsiri, D. W. Greening and R. J. Simpson, *Nature Reviews Clinical Oncology*, 2018, **15**, 617–638.

70 N. Dilsiz, *Future Science OA*, 2020, **6**, FSO465.

71 D. Wu, J. Yan, X. Shen, Y. Sun, M. Thulin, Y. Cai, L. Wik, Q. Shen, J. Oelrich, X. Qian, K. L. Dubois, K. G. Ronquist, M. Nilsson, U. Landegren and M. Kamali-Moghaddam, *Nature Communications*, 2019, **10**, 3854.

72 S. Sharma, K. Das, J. Woo and J. K. Gimzewski, *Journal of The Royal Society Interface*, 2014, **11**, 20131150.

73 T. Huang and C.-X. Deng, *International journal of biological sciences*, 2019, **15**, 1–11.

74 C. Carrasco, A. Carreira, I. A. T. Schaap, P. A. Serena, J. Gómez-Herrero, M. G. Mateu and P. J. de Pablo, *Proceedings of the National Academy of Sciences*, 2006, **103**, 13706–13711.

75 M. Hernando-PÃ©rez, R. Miranda, M. Aznar, J. L. Carrascosa, I. A. T. Schaap, D. Reguera and P. J. de Pablo, *Small*, 2012, **8**, 2366–2370.

76 S. Kwon, W. Yang, D. Moon and K. S. Kim, *J Cancer*, 2020, **11**, 5403–5412.

77 V. Swaminathan, K. Mythreye, E. T. O'Brien, A. Berchuck, G. C. Blobe and R. Superfine, *Cancer Research*, 2011, **71**, 5075–5080.

78 W. Xu, R. Mezencev, B. Kim, L. Wang, J. McDonald and T. Sulchek, *PLOS ONE*, 2012, **7**, 1–12.

79 J. Guck, S. Schinkinger, B. Lincoln, F. Wottawah, S. Ebert, M. Romeyke, D. Lenz, H. M. Erickson, R. Ananthakrishnan, D. Mitchell, J. Käs, S. Ulvick and C. Bilby, *Biophysical Journal*, 2005, **88**, 3689–3698.

80 M. Plodinec, M. Loparic, C. A. Monnier, E. C. Obermann, P. Zanetti-Dallenbach, Rosannaand Oertle, J. T. Hyotyla, U. Aebi, M. Bentires-Alj, R. Y. H. Lim and C.-A. Schoenenberger, *Nature Nanotechnology*, 2012, **7**, 757–765.

81 D. Chanda, E. Otoupalova, K. P. Hough, M. L. Locy, K. Bernard, J. S. Deshane, R. D. Sanderson, J. A. Mobley and V. J. Thannickal, *American journal of respiratory cell and molecular biology*, 2019, **60**, 279–288.

82 P.-G. Moon, J.-E. Lee, Y.-E. Cho, S. J. Lee, Y. S. Chae, J. H. Jung, I.-S. Kim, H. Y. Park and M.-C. Baek, *Oncotarget*, 2016, **7**, 40189–40199.

83 B. H. Sung, T. Ketova, D. Hoshino, A. Zijlstra and A. M. Weaver, *Nature communications*, 2015, **6**, 7164–7164.

84 A. Purushothaman, S. K. Bandari, J. Liu, J. A. Mobley, E. E. Brown and R. D. Sanderson, *Journal of Biological Chemistry*, 2016, **291**, 1652–1663.

85 R. E. Sexton, G. Mpilla, S. Kim, P. A. Philip and A. S. Azmi, *Seminars in Cancer Biology*, 2019, **54**, 131–137.

86 A. Datta, H. Kim, M. Lal, L. McGee, A. Johnson, A. A. Moustafa, J. C. Jones, D. Mondal, M. Ferrer and A. B. Abdel-Mageed, *Cancer Letters*, 2017, **408**, 73–81.

87 T. Hikita, A. Kuwahara, R. Watanabe, M. Miyata and C. Oneyama, *Scientific Reports*, 2019, **9**, 3265.

88 A. Thakur, G. Qiu, C. Xu, X. Han, T. Yang, S. P. NG, K. W. Y. Chan, C. M. L. Wu and Y. Lee, *Science Advances*, 2020, **6**, eaaz6119.

89 T. Yoshida, T. Ishidome and R. Hanayama, *Current Protocols in Cell Biology*, 2017, **77**, 3.45.1–3.45.18.

90 Y. Zhou, B. Zhou, L. Pache, M. Chang, A. H. Khodabakhshi, O. Tanaseichuk, C. Benner and S. K. Chanda, *Nature Communications*, 2019, **10**, 1523.

91 T. Fukuma, M. Kimura, K. Kobayashi, K. Matsushige and H. Yamada, *Review of Scientific Instruments*, 2005, **76**, 053704.

92 T. Fukuma, Y. Ueda, S. Yoshioka and H. Asakawa, *Phys. Rev. Lett.*, 2010, **104**, 016101.

93 T. Fukuma, K. Onishi, N. Kobayashi, A. Matsuki and H. Asakawa, *Nanotechnology*, 2012, **23**, 135706.

94 J. L. Hutter and J. Bechhoefer, *Review of Scientific Instruments*, 1993, **64**, 1868–1873.

95 T. Fukuma and R. Garcia, *ACS Nano*, 2018, **12**, 11785–11797.

96 J. E. Sader and S. P. Jarvis, *Applied Physics Letters*, 2004, **84**, 1801–1803.

97 B. B. Akhremitchev and G. C. Walker, *Langmuir*, 1999, **15**, 5630–5634.

98 P. D. Garcia and R. Garcia, *Biophysical Journal*, 2018, **114**, 2923–2932.

99 F. Rico, P. Roca-Cusachs, N. Gavara, R. Farré, M. Rotger and D. Navajas, *Phys. Rev. E*, 2005, **72**, 021914.